Article

Selective Synthesis of Defect-Rich LaMnO₃ by Low-Temperature Anion Cometathesis

Gia Thinh Tran, Allison Wustrow, Daniel O'Nolan, SongSheng Tao, Christopher J. Bartel, Tanjin He, Matthew J. McDermott, Brennan C. McBride, Karena W. Chapman, Simon J. L. Billinge, Kristin A. Persson, Gerbrand Ceder, and James R. Neilson*
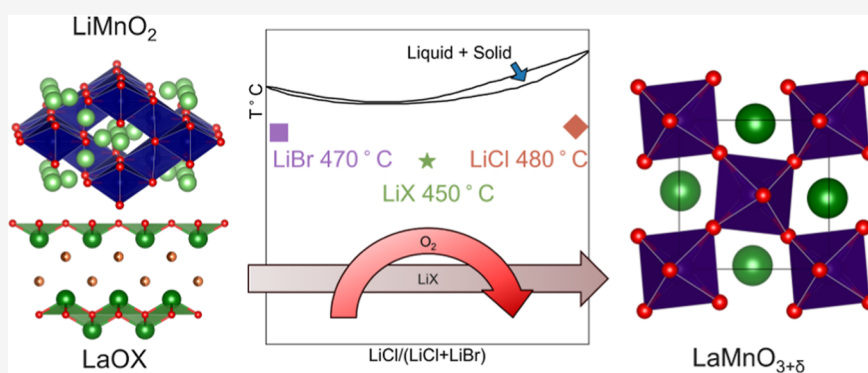
Read Online

ACCESS | Metrics & More | Article Recommendations | Supporting Information

ABSTRACT: The synthesis of complex oxides at low temperatures brings forward aspects of chemistry not typically considered. This study focuses on perovskite LaMnO₃, which is of interest for its correlated electronic behavior tied to the oxidation state and thus the spin configuration of manganese. Traditional equilibrium synthesis of these materials typically requires synthesis reaction temperatures in excess of 1000 °C, followed by subsequent annealing steps at lower temperatures and different $p(O_2)$ conditions to manipulate the oxygen content postsynthesis (e.g., $LaMnO_{3+x}$). Double-ion exchange (metathesis) reactions have recently been shown to react at much lower temperatures (500−800 °C), highlighting a fundamental knowledge gap for how solids react at lower temperatures. Here, we revisit the metathesis reaction, $LiMnO_2 + LaOX$, where X is a halide or mixture of halides, using in situ synchrotron X-ray diffraction. These experiments reveal low reaction onset temperatures (ca. 450−480 °C). The lowest reaction temperatures are achieved by a mixture of lanthanum oxyhalide precursors: $2 LiMnO_2 + LaOCl + LaOBr$. In all cases, the resulting products are the expected alkali halide salt and defective $La_{1−\epsilon}Mn_{1−\epsilon}O_3$, where $\epsilon = x/(3 + x)$. We observe a systematic variation in defect concentration, consistent with a rapid stoichiometric local equilibration of the precursors and the subsequent global thermodynamic equilibration with O_2 (g), as revealed by computational thermodynamics. Together, these results reveal how the inclusion of additional elements (e.g., Li and a halide) leads to the local equilibrium, particularly at low reaction temperatures for solid-state chemistry.

INTRODUCTION

Our understanding of how solid-forming reactions proceed and are controlled is limited by intermediate reaction temperatures. For reactions below ca. 300 °C, we know that some ions of low charge and/or size can selectively diffuse,[1] thus enabling the synthesis of highly out-of-equilibrium phases such as $LaNiO_2$[2] and $SrFeO_2$[3] with square planar transition-metal coordination geometries or unusual oxidation states.[4] This contrasts the apparent nonselective diffusion down concentration gradients that occur at elevated temperatures ($T > 800$ °C).[5] Solid-state metathesis reactions, while originally explored for their highly exothermic nature to synthesize refractory materials, can be used to synthesize materials requiring far milder conditions,[6] such as in the synthesis of metastable chalcogenides ($T_{rxn} <$

150 °C)[7] or the alkali-dependent synthesis of different yttrium manganese oxides ($500 < T_{rxn} < 800$ °C).[8,9] In these oxide-forming reactions, it has been shown that the precursor polymorph influences how the reaction proceeds.[10] Furthermore, cometathesis reactions with mixtures of "spectating" ions (e.g., the alkali or alkaline earth elements) exhibit cooperative reactivity highlighted by a reduced reaction temperature (e.g.,
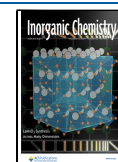
$MgMn_2O_4 + CaMn_2O_4 + 4$ YOCl)[11] and even polymorph selectivity.[12] However, many simple questions remain concerning the general applicability and understanding of the progression toward equilibrium of these reactions.

$LaMnO_3$, a focus of this study, has been studied for its ability to accommodate a range of defect concentrations and its resulting physical properties in the nonstoichiometric phases. The phase is often mixed valence, and control over the Mn valence gives rise to the highly nonlinear "colossal magneto-resistance" effect.[13] While the Mn valence can be modified via aliovalent substitution (e.g., Sr^{2+} for La^{3+}), the reaction temperature and exposure to different oxygen partial pressures give rise to significant cation vacancies and nonstoichiometry that can also produce mixed valence Mn.[14−16] For highly oxidized compounds ($x \geq 0.09$), the prototypical $Pnma$ tilted perovskite structure undergoes a phase transition to the $R3c$ perovskite crystal structure.[15] While this paper will refer to the nonstoichiometric composition as $LaMnO_{3+x}$ it is important to articulate that the excess oxygen is accommodated via cation vacancies and not oxygen interstitials: $La_{1-\epsilon}Mn_{1-\epsilon}O_3$, where $\epsilon = x/(3 + x)$; however, the concentration of La and Mn vacancies need not be equivalent.[15] Collectively, we will refer to this phase, stoichiometric and nonstoichiometric, as $LaMnO_3$; we only refer to the stoichiometric compound where specifically noted.

The oxygen content in $LaMnO_3$ relies on the chemical potential of oxygen, which is temperature-dependent. A survey of the synthesis conditions of $LaMnO_3$ reveals that high temperatures limit the highest chemical potential of oxygen accessible under ambient pressure, which in turn reflects the stoichiometry of $LaMnO_3$ and, therefore, the properties. According to 61 synthesis procedures extracted from the experimental literature for $LaMnO_3$, the reaction temperatures range from ca. 600 to ca. 1500 °C, with most reactions taking place between 1000 and 1300 °C (Figure 1). Typical precursors include manganese oxides and La_2O_3.[17] However, initial metathesis[18] and "assisted" metathesis[19] reactions employing $LiMnO_2$ as a precursor reported relatively high reaction temperatures (ca. 800−850 °C) in contrast to our previous work.[11,12] Most synthetic conditions require an initial high-temperature reaction (at least 800 °C or above), followed by annealing at lower temperatures under varied oxygen partial pressures to adjust the stoichiometry. Here, we present a reaction temperature as low as 450 °C (star in Figure 1). The low reaction temperature facilitates access to a local equilibrium with higher oxygen chemical potential than high-temperature syntheses, thus allowing for a wider range of $LaMnO_3$ stoichiometries.

Here, we specifically study and discuss the ternary metathesis reactions

$$LiMnO_2 + LaOX \rightarrow LiX + LaMnO_3 \quad (1)$$

where X = Cl, Br. The primary questions addressed are (1) how does the reaction temperature relate to the byproduct salt phase diagram and its solidus and (2) how do the local chemical potentials of the reactants and subsequent intermediates impart selectivity over the final reaction products. $LiMnO_2$ is combined with stoichiometric equivalents of LaOCl, LaOBr, or the mixture of 0.5 equiv of LaOCl + 0.5 equiv of LaOBr to produce $LaMnO_3$. Using synchrotron X-ray diffraction with a modified capillary furnace, a series of in situ and postheated isothermal X-ray diffraction patterns (ex post facto) show the influence on the defect-mediated reaction
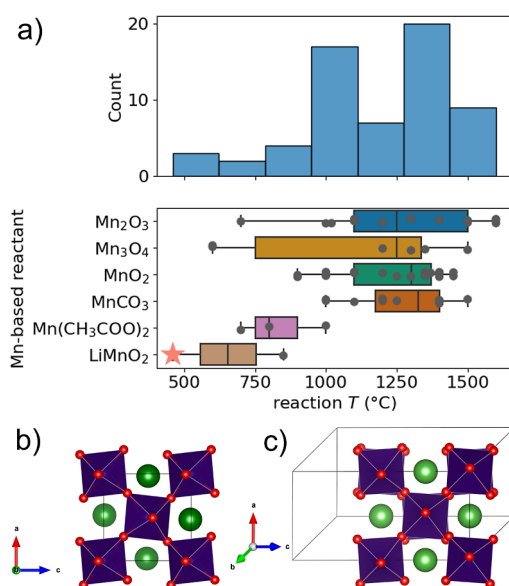

Figure 1. (a) Top: Histogram of reported $LaMnO_3$ syntheses across a range of reaction temperatures. Most report a temperature of at least 800 °C or above. The star marks the lowest reaction temperature that is reported herein. Bottom: Distribution of reaction temperatures as sorted by different Mn-containing precursors used to synthesize $LaMnO_3$ at given temperatures. Mn_3O_4 and $Mn(CH_3COO)_2$ precursors require oxidation and appear with lower reaction temperatures. (Crystal structure representations of (b) $R3c$ and (c) $Pnma$ $LaMnO_3$.)

pathway. We observe that the combination of halides (i.e., anion cometathesis) lowers the effective reaction temperature. Crystallographic analysis of the intermediate phases suggests that the reaction proceeds by propagating point defects in the different reactive phases. It appears that the local chemical potentials initially push the reaction toward stoichiometric $LaMnO_3$, which then equilibrates to an oxidized $LaMnO_{3+x}$ product. Longtime points and higher temperature reactions are consistent with experiments performed at high temperatures and high equilibrium oxygen partial pressures (Figure S1).

■ EXPERIMENTAL METHODS

Precursor Synthesis. 0.3 g of lanthanum oxyhalides were synthesized via solid-state synthesis. Lanthanum oxide was mixed with stoichiometric amounts plus 10 mol % excess of the respective ammonium halide salt (Acros Organics 99.9%) with a mortar and pestle. The mixture was then placed in an alumina crucible to heat in air at 600 °C for 3 h with heating and cooling rates of 10 °C/min. 5 g of $LiMn_2O_4$ was synthesized by reacting stoichiometric amounts of Li_2CO_3 (Baker, 99.3%) and Mn_2O_3. Mn_2O_3 was synthesized by heating $MnCO_3$ (Sigma-Aldrich, 99.9%) in an alumina crucible in air at 850 °C for 12 h with heating and cooling rates of 10 °C/min. The Li_2CO_3 and Mn_2O_3 powders were mixed using a mortar and pestle, pelleted, and heated in an alumina crucible at 800 °C for 24 h with heating and cooling rates of 10 °C/min.[20] To prepare tetragonal $LiMnO_2$, $LiMn_2O_4$ powder was refluxed under nitrogen in a 4 M LiI solution in acetonitrile (Alfa Aesar, 99.9%) where the overall Li/Mn ratio was 6:1. The reflux was performed by using an oil bath. After reflux, the powder was filtered and washed with acetonitrile to remove residual LiI and I_2 before it was dried under vacuum at 80 °C.[21]

Bulk Reactions. Bulk reactions were prepared by mixing stoichiometric amounts of $LiMnO_2$ and lanthanum oxyhalides in a mortar and pestle for 15 min in an argon glovebox with ≤1 ppm of O_2 and ≤1 ppm of H_2O. The homogenized mixture was then pelleted, placed in a cylindrical alumina crucible, and sealed in an evacuated

quartz ampule (≤20 mTorr). Reactions were heated at 10 °C/min to the dwell temperature (600 °C) to ensure product formation within 4 h. Sample product identification was verified with laboratory powder X-ray diffraction (PXRD) data collected on a Bruker D8 Discover diffractometer using Cu Kα radiation and a Lynx Eye XE-T position sensitive detector (Figure S1).

In Situ and Ex Post Facto SXRD Reactions. Synchrotron X-ray diffraction (SXRD) data were collected at beamline 28-ID-2 at National Synchrotron Light Source II at Brookhaven National Laboratory. Data for the reactions were obtained with a gradient furnace, where each horizontal position is calibrated and defined to a temperature.[22] The gradient furnace ensures its temperature gradient through scaling densities of heating elements along a quartz capillary. Samples were packed into 1.1 mm outer diameter, 0.9 mm inner diameter quartz capillaries (Friedrich & Dimmock) in an argon-filled glovebox and carefully flame-sealed under vacuum. This capillary was then brought out of the glovebox and quickly sealed under vacuum (≤20 mTorr). Calibration of the detector curvature was performed using CeO$_2$ at all points along the gradient furnace using pyFAI.[23] SXRD data were collected on a PerkinElmer plate detector at a 1400 mm distance and 1480 mm at two different visits to the light source. Using a PID-controlled power source, a horizontal temperature range of 300−800 °C along the capillary was created. The temperature at a given position (1 mm increments) was calibrated with NaCl and its thermal expansion.[24] Samples were held at temperatures for 40 min twice for two separate time points. Samples were then cooled at an approximately 5 °C/min rate. Ex post facto diffraction data were collected after the heating experiment with a wavelength of 0.1949 Å at ambient temperatures.

Quantitative Analysis of Diffractive Data. Quantitative phase analysis of X-ray diffraction data was performed using the Rietveld method with the TOPAS v6 software package. The following assumptions were made for consistent analysis: Atomic displacement parameters were fixed to a value of $B = 1$ Å^2, and peak broadening is primarily modeled via crystal size broadening using a refined Lorentzian function. Data from ex post facto SXRD runs are plotted as weight fractions.

Computational Methods. Formation enthalpies ($T = 0$ K) were obtained with density functional theory (DFT) using the r2SCAN meta-GGA density functional.[25,26] Starting structures were obtained either from the Materials Project database[27] or from the XRD-refined structures synthesized in the present work. All structures were optimized using the Vienna Ab initio Simulation Package and the projector augmented wave method.[28] A plane wave energy cutoff of 520 eV and 1000 k-points per reciprocal atom were used for all calculations. Gibbs free energies of formation, $\Delta G_f(T)$, were obtained for each solid compound by combining the DFT-calculated formation enthalpies with vibrational and configurational contributions to the entropy. The vibrational entropy contribution was determined using the machine-learned descriptor introduced by Bartel et al.[29] Configurational entropy was estimated by considering the entropy of mixing for an ideal solid solution for any site with partial occupancies. Gibbs formation energies, including DFT-computed ambient temperature formation enthalpies, model-predicted vibrational entropies, and ideal mixing configurational entropies, were then used to compute all of the Gibbs reaction energies presented in this work. Reaction energies were normalized to yield 1 mol of LaMnO$_3$.

Predominance diagrams were constructed using the chemical potential diagram approach described by Yokokawa[30] and implemented in a previous work.[9] Thermodynamic data for the predominance diagrams were acquired from the Materials Project (MP), version 2022.10.28. Gibbs free energies of formation for temperatures $T > 0$ K were approximated from MP data using the aforementioned machine-learned descriptor developed by Bartel et al.[29] According to our computed data, LaMnO$_3$ is not predicted to be stable at any temperature. Thus, LaMnO$_3$ was manually stabilized (energy lowered until brought onto the hull) to illustrate its approximate position on the predominance diagram. The predominance diagrams were constructed as two-dimensional projections in the $\mu_{La}-\mu_O$ space from the full five-dimensional (La−Mn−O−Li−X)

chemical potential diagram for the system. Boundaries from the higher-dimensional space (e.g., LiMnO$_2$ in the La−O predominance diagram) are plotted as half-space intersections as previously described.[9] Oxygen chemical potentials marked on the predominance diagram were estimated for different pressures as $\mu_O = 0.5 k_b T \ln P_{O_2}$, where P_{O_2} is the partial pressure of the O$_2$ gas in atm. These oxygen chemical potentials represent differences from the standard state chemical potential of oxygen, μ_O^0, which is taken to be 0 eV at $P_{O_2} = 1$ atm. An atmospheric oxygen partial pressure of 0.1731 atm was assumed for the air in Fort Collins, CO, corresponding to an elevation of ≈5000 ft.

■ RESULTS AND DISCUSSION

Ex situ synchrotron powder X-ray diffraction indicates that the temperature at which LaMnO$_3$ forms falls below the solidus of the LiCl−LiBr phase diagram, with the lowest temperature reaction being that containing mixed halogen precursors: LiMnO$_2$ + 0.5 LaOCl and 0.5 LaOBr. Using the gradient furnace (see the Experimental Methods), the product distributions of the ex post facto reactions were determined using the Rietveld method and are plotted in Figure 2.
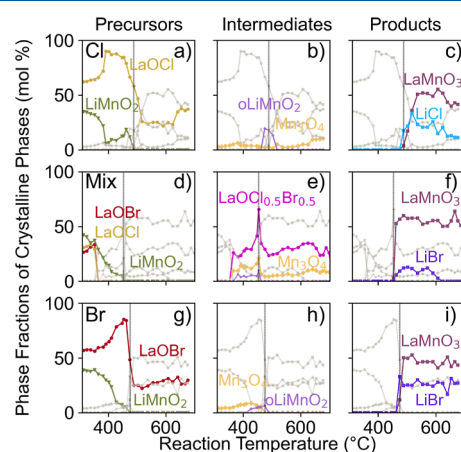

Figure 2. Phase fractions of crystalline phases from isothermal reactions performed at different temperatures in a gradient furnace from powder synchrotron X-ray diffraction data for the reaction of (a−c) LaOCl + LiMnO$_2$ (d−f) 0.5 LaOCl + 0.5 LaOBr + LiMnO$_2$, and (g−i) LaOBr + LiMnO$_2$. Formation temperatures are marked as vertical solid gray lines. The lowest reaction temperature (450 °C) for the formation of LaMnO$_3$ occurs with 0.5 LaOCl + 0.5 LaOBr + LiMnO$_2$, while all observed LaMnO$_3$ formation temperatures are approximately 50 °C below the melting point temperature of the salt.

Qualitatively, the phase distributions are illustrated by their identity as precursors, intermediates, and products. The intermediate phases observed include orthorhombic LiMnO$_2$ and a phase consistent with a spinel phase, presuming Mn$_3$O$_4$. For the mixed halide cometathesis reaction, solid-solution LaOCl$_{0.5}$Br$_{0.5}$ forms. In all three reactions studied, the alkali halide salt forms at the same nominal reaction temperature (i.e., capillary position) as LaMnO$_3$; the temperature for this reaction onset is approximately 50 °C below the melting point for the LiCl−LiBr solidus (Figure 3). The lowest LaMnO$_3$ formation temperature is observed for the anion cometathesis reaction (LaOCl onsets at ca. 490 ± 14 °C; LaOBr onsets at ca. 470 ± 13 °C; and the LaOCl/LaOBr mixture onsets at ca. 450 ± 7.3 °C). The uncertainties are the difference between the onset temperature and the temperature of the next temperature scan. Product formation at onset temperature
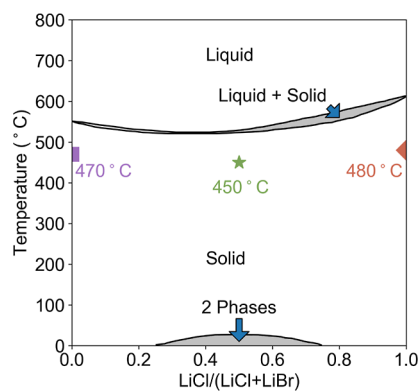
Figure 3. Equilibrium phase diagram of the LiCl−LiBr system. LaMnO$_3$ onset formation temperatures of each metathesis reaction are marked (Cl as red diamond, Br as purple square, cometathesis as green star).[31] The onset temperature in the cometathesis reaction is approximately 100 °C below the solidus line.

below the nascent salt solidus has been previously observed in alkali and alkaline earth cometathesis reactions (e.g., MgMn$_2$O$_4$ + CaMn$_2$O$_4$ + 4YOCl),[11,12] and we proposed that the abrupt onset is consistent with the surface melting of the nascent salt just as it starts to form. Surface melting is distinct from the formation of a bulk molten alkali halide as the crystalline salt is observed by in situ diffraction at the onset temperature and adiabatic self-heating does not appear to be sufficient to cause melting at the interface.[11] Here, it is clear that the mixing of anions produces a similar effect consistent with surface melting of the nascent alkali halide salt at the interface, akin to cometathesis, acting to facilitate LaMnO$_3$ formation.

Ex situ synchrotron powder X-ray diffraction shows that the metathesis reactions produce LaMnO$_3$ with a reduced unit cell volume relative to the stoichiometric unit cell, most consistent with cation vacancies (e.g., La$_{1-\epsilon}$Mn$_{1-\epsilon}$O$_3$). The unit cell volume of LaMnO$_3$ was calculated from Rietveld refinements at room temperature and is plotted as a function of reaction temperature in Figure 4. In all cases, the structure described by the *Pnma* space group provides the best fit to the data. The rhombohedral *R3c* structure often found for highly oxidized LaMnO$_{3+x}$[15] or Li-substituted LaMn$_{1-3x}$$^{3+}Mn_{2x}$$^{4+}Li_xO_3$ did not provide a better fit to the data (see Figure S5 and the discussion therein).[32] The unit cell of LaMnO$_3$ produced at
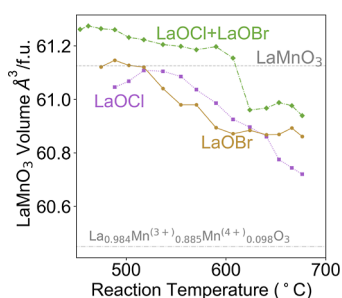

Figure 4. Unit cell volume of LaMnO$_3$ as a function of the temperature determined by Rietveld refinements. Single anion 0.5 LaOCl/Br + LiMnO$_2$ and 0.5 LaOCl + 0.5 LaOBr + LiMnO$_2$ reactions yield a higher unit cell volume than the phase formed by solid solution metathesis. Topfer reports stoichiometric LaMnO$_3$ with a volume of 61.05 Å^3 (gray dashed line) and La$_{0.984}$Mn$_{0.885}$$^{3+}Mn_{0.098}$$^{4+}O_3$ with 60.40 Å^3 (gray dashed-dotted line).[14]

higher reaction temperatures is smaller relative to that at lower reaction temperatures. A comparison of the observed unit cell volumes with previous studies[15,33] reveals that the product from the LaOCl/LaOBr cometathesis reaction is nearly stoichiometric at the lowest reaction formation temperature (compared to 61.05[15] to 61.2 Å^3/fu[33]). Yet, at higher reaction temperatures, the unit cell volume is smaller, as previously attributed to the presence of a smaller Mn^{4+} cation and cation vacancies.[15] One would typically expect reactions at higher temperatures to be less oxidizing due to the reduced chemical potential of O$_2$(g) at elevated temperatures. The observations here are counter to this expectation.

A closer examination of in situ PXRD collected at different time points during the reaction as it happens reveals a time-dependent variation of the unit cell volume of LaMnO$_3$. The gradient furnace used in these experiments permits practical analysis of the time-dependent change in the lattice parameters at constant temperature, as summarized in Table 1. Upon its

Table 1. Volumes of LaMnO$_3$ per Formula Unit from the In Situ and Ex Situ LaOBr + LiMnO$_2$ Metathesis Reaction in Relation to Temperature and Time^a

temperature (°C)	time (min)	volume (Å^3/fu)
488°C	20 min	61.662(1)
488°C	40 min	63.095(1)
ex post facto 25°C	ex post facto	61.145(1)
570°C	20 min	62.965(1)
570°C	40 min	63.118(1)
ex post facto 25 °C	ex post facto	62.552(1)

^{a}LaMnO$_3$'s unit cell volume increases above the onset temperature as well as over time. The unit cell shrinks upon cooling.

initial formation at the lowest temperature (i.e., at the onset), the unit cell volume of LaMnO$_3$ is close to the volume of stoichiometric LaMnO$_3$. After 20 min at constant temperature, the unit cell volume increases: at 488 °C, the volume increases from 61.662(1) to 63.095(1) Å^3/fu. From the benefit of the gradient furnace, the isothermal nature of this time-dependent change rules out thermal expansion of LaMnO$_3$. To further rule out thermal expansion, Miyoshi et al. calculated a linear thermal expansion coefficient of $(1.06(1)) \times 10^{-5}$;[34] the expected volume from thermal expansion of stoichiometric LaMnO$_3$ is only 61.999(1) Å^3/fu at 488 °C, employing $\Delta V/V = 3\alpha\Delta T$ and the initial volume of 61.1 Å^3. It is currently unclear why the volume initially increases to such a large value. The same trend in increasing unit cell volume with prolonged time is also observed at 570 °C. The unit cell after cooling is smaller than what is predicted from thermal contraction of the 40 min time point measured at elevated temperature: at 488 °C, one would expect 63.095(1) Å^3 to contract to 62.179(1) Å^3 (61.145 Å^3 observed); at 570 °C one would expect 63.118(1) Å^3 to contract to 62.043(1) Å^3 (62.552 Å^3 observed) instead of the observed volumes (Table 1). Therefore, we turn to computationally derived phase diagrams to address the equilibration of the precursors with the evolving atmosphere at these low temperatures.

To explain the trends in LaMnO$_3$ unit cell volumes as a function of reaction temperature and time, we analyze the computationally derived chemical equilibrium at reaction interfaces and of the overall equilibrium. To understand the equilibrium of a reaction interface, it is useful to employ a predominance diagram viewed along the axes of the elemental

chemical potentials that define the system. Since the local interface has a nearly infinite reservoir of each elemental component, the intensive variable of chemical potential is more reliable than the extensive variable of the average concentration.[30] The dominant diagram shown in Figure 5 illustrates
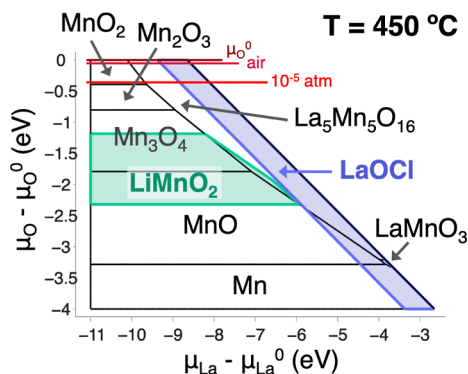

Figure 5. DFT-derived predominance diagram of lanthanum and oxygen chemical potentials shown at 450 °C referenced to their standard elemental states. For the La−Li−Mn−O−Cl system, a description of the reaction energetics is provided in the Supporting Information, with specific elaboration of the relative contribution of the entropy attributed to solid solution formation. Pressures of oxygen gas (red lines) highlight the chemical potential that is expected at 1 atm, partial oxygen pressure in air, and partial oxygen pressure in an argon atmosphere (10 ppm). LiMnO$_2$ (green) and LaOCl (blue) are visible as projected planes across the chemical potential space. All projected phases overlap with the overoxidized phase, La$_5$Mn$_5$O$_{16}$. Only LaOCl overlaps with LaMnO$_3$. La$_5$Mn$_5$O$_{16}$ should be treated as encompassing all stable oxidized LaMnO$_3$ states rather than a stoichiometrically defined compound.

the La−Mn−O chemical potential space viewed in the μ_{La}−μ_O axes. It also illustrates the intersection of LiMnO$_2$ and LaOCl from the high-dimensional La−Mn−O−Li−Cl chemical potential space, as previously described.[9,35] This phase diagram is derived from computationally tractable analogues of the experimental nonstoichiometric phases. For example, the ordered, cation-deficient phase, La$_5$Mn$_5$O$_{16}$, encompasses overlapping ranges of stability for the near continuum of cation-deficient LaMnO$_3$ phases. The large stability field of La$_5$Mn$_5$O$_{16}$ reflects the significant propensity for oxidation via the cation deficiency of stoichiometric LaMnO$_3$, which itself is visible only at low oxygen chemical potentials.

We previously illustrated that reactant−product adjacency on chemical potential diagrams can rationalize selective phase formation based on the local equilibration of chemical potentials across the reactant/product interfaces.[9] In the phase equilibria illustrated in Figure 5, LaOCl and LiMnO$_2$ both share a stable boundary with La$_5$Mn$_5$O$_{16}$, suggesting that nucleation of an oxidized La$_5$Mn$_5$O$_{16}$ at the LaOCl/LiMnO$_2$ interface will lead to local thermodynamic equilibrium that pins the local oxygen chemical potential to a rather low value. If one draws the shortest distance in chemical potential space between LaOCl and LiMnO$_2$, this is near an oxygen chemical potential of μ_O−$\mu_O^0 \approx -2$ eV. If we assume that "La$_5$Mn$_5$O$_{16}$" represents a continuum of nonstoichiometric LaMnO$_3$ phases, then we would expect this phase to have the largest unit cell volume at the lowest oxygen chemical potentials, consistent with the observed in situ unit cell volumes (Table 1) at short times and low temperatures.

However, the oxygen chemical potential of the reaction environment is significantly higher and promotes the formation of more oxidized LaMnO$_3$ with a smaller unit cell volume. In these reactions performed in evacuated capillaries and ampules, the $p(O_2) \approx 10^{-5}$ atm, for which μ_O−$\mu_O^0 = 0.5k_bT \ln(p/p^0) = -0.458$ eV at 650 °C. If we assume that the presence of LiMnO$_2$ pins the local chemical potential between the values of μ_O−$\mu_O^0 = -1.2$ and -2.25 eV (e.g., its stability window along the μ_O−μ_O^0 axis), then after LiMnO$_2$ is consumed, the oxygen chemical potential is no longer pinned to those values. As such, the system can equilibrate with that of the surrounding atmosphere, which is at a much higher value (-0.458 eV). This analysis of the local thermodynamics at the reaction interfaces explains the time- and temperature-dependent shift in the unit cell volumes of LaMnO$_3$. At the higher temperatures studied here, equilibration with the atmosphere becomes noticeable due to the enhanced solid-state oxygen diffusion, which is severely hampered at lower temperatures. Together, we propose that the chemical potential of the precursors defines the local equilibrium of the reaction by way of their respective stability windows with respect to the elemental chemical potentials.

Going further, a crystallographic examination of the evolution of other phases in the reaction mixture provides corroborating evidence of the progression from a local to bulk equilibrium at higher reaction temperatures. The ex post facto analysis reveals that tetragonal LiMnO$_2$ undergoes a phase transformation into a phase that is indexed as the more thermodynamically stable orthorhombic LiMnO$_2$ polymorph *Pmnm* as well as the formation of a phase that is best indexed as tetragonal spinel consistent with Mn$_3$O$_4$ ($I4_1/amd$). However, the specific stoichiometry of that phase remains somewhat ambiguous due to the ability of spinels to accommodate significant defects,[10] as detailed in the Supporting Information. In our previous study of the metathesis reactions LiMnO$_2$ + YOCl, we observed charge disproportionation of manganese ions into two different defect spinels, such that cubic spinel "LiMn$_2$O$_4$" accumulates oxidized Mn$^{3+\delta}$ cations and the tetragonal spinel, "Mn$_3$O$_4$" accumulates reduced Mn$^{3-\delta}$ cations.[10,36] In this study, we only detect the presence of a tetragonal spinel, Mn$_3$O$_4$, which could be present to offset the presence of the overoxidized LaMnO$_{3+x}$ or is itself defective with only Mn^{3+} present in the mixture.

LaOX are known to accommodate nonstoichiometry through ordered and disordered defects. Crystallographic analysis of the LaOX phases during the reaction does not reveal gross defect nonstoichiometry but perhaps some subtle deviations that give insights into the reaction path. In the anion cometathesis reaction, LaOCl and LaOBr react to form the solid solution LaOCl$_{0.5}$Br$_{0.5}$. As defects are known to influence the unit cell volume, the volumes of LaOX were extracted from the ex post facto diffraction data by using the Rietveld method. In Figure 6, the LaOX average volume is computed by adding together the unit volumes of the observed LaOX phases (i.e., LaOCl, LaOBr, Cl-rich solid solution, Br-rich solid solution; then LaOCl$_{0.5}$Br$_{0.5}$ above 370 °C) and dividing by the total number of phases present (four or five), assuming an equimolar mixture of phases. The unit cell volumes of LaOCl and LaOBr during single anion metathesis reactions stay relatively consistent at 116.95 and 127.88 Å^3, respectively, as a function of temperature. Anion cometathesis reactions reveal a discontinuous jump in LaOX volume as solid solution LaOCl$_{0.5}$Br$_{0.5}$ forms. Once formed, the volume of LaOCl$_{0.5}$Br$_{0.5}$
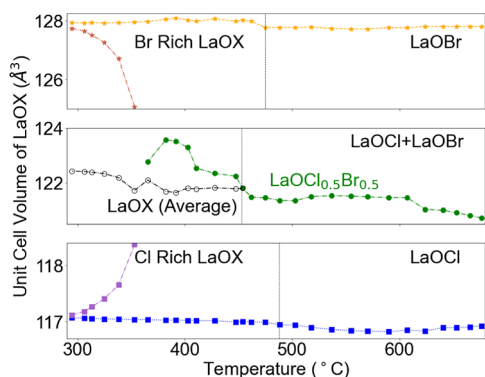
Figure 6. Unit cell volume of LaOX as a function of temperature, determined by Rietveld refinements. The unit cell volume of each end member system are shown in comparison to the unit cell volume of each end member as it reacts to form solid solutions (purple and red). The unit cell volume of $LaOCl_{0.5}Br_{0.5}$ is shown compared to the average of all LaOX species. The volumes of the LaOX phases prior to the formation of $LaOCl_{0.5}Br_{0.5}$ have been averaged and are represented as one volume. The solid solution decrease over the course of the reaction after the product onset temperature (indicated with the gray vertical lines) well below the literature value while single halide phases experience less volume changes. Residual LaOX phases are detected above the reaction onset temperatures.

decreases to 120.7 $Å^3$ as the temperature increases. According to Vegard's law, the theoretical unit cell volume is predicted to be 121.9 $Å^3$.

The continual decrease of the unit cell volume of solid-solution $LaOCl_{0.5}Br_{0.5}$ suggests that cometathesis propagates through defect formation mechanisms different from those of single-anion methathesis reactions. We explore the following three hypotheses: (1) cation intercalation into the van der Waals gap during reaction with $LiMnO_2$, (2) asymmetric anion reactivity with a greater loss of bromine than chlorine, and (3) preferential reaction of halogen over oxygen out of $LaOCl_{0.5}Br_{0.5}$. With the first hypothesis, one would expect an increase of the c axis with the intercalation in metal oxychlorides,[37,38] but the opposite is observed. The second hypothesis is consistent with the observed lattice parameter of the salt byproduct LiX that equilibrates to 5.35(1) Å, which agrees with the expected value for $LiCl_{0.4}Br_{0.6}$ predicted with Vegard's law. Finally, we return to the third hypothesis, in which the halogen preferentially deintercalates over oxygen. This hypothesis is rationalized by two factors. In the solid-solution $LaOCl_{0.5}Br_{0.5}$, the local strain from having two different halide radii likely decreases the effective bond dissociation energy of the halogen relative to the oxygen.[39] Second, as La^{3+} is removed from the crystal during reaction, it can be equivalently charge compensated with the simultaneous removal of different amounts of oxygen and halogen. For each La^{3+} removed, this corresponds to either one O and one X (1:1), one and a half O (1.5:0, actually three O for every two La), or three X (0:3). If we assume that all defect procedures are equally favorable, then the total ratio is (2.5:4). Therefore, one expects a higher rate of halogen removal solely on the basis of the stoichiometric ratios. Both factors would lead to increased reactivity of the halogen, which is consistent with the observations. This reveals the atomistic origin of the variation of the chemical potential within a single phase.

CONCLUSIONS

Metathesis reactions provide the ability to control the local equilibrium of reactions at their onset, which then reach global equilibrium with reaction progression. Specific to this study, the role of anion cometathesis (i.e., a mixture of like precursors) is identical to that of cation cometathesis (i.e., mixing halogens is the same as mixing alkalis). In detail, the reaction of $LiMnO_2$ + LaOX, where X is Cl, Br, or an equimolar mixture, the product $LaMnO_{3+x}$ forms with excess oxygen relative to the metal cations. By understanding the chemical potential landscape, we can enable more synthetic control in solid-state syntheses, as atomistic defect species in functional materials often control macroscopic properties. Further efforts to understand defect formation in low temperature synthesis will assist us in the pursuit of a complete selective synthesis.

ASSOCIATED CONTENT

Ⓢ Supporting Information

The Supporting Information is available free of charge at https://pubs.acs.org/doi/10.1021/acs.inorgchem.3c03305.

List of references used in Figure 1;illustration of laboratory X-ray diffraction data of the product from quenched ex situ, bulk reactions of anion cometathesis; description of energy calculations of the reaction, LaOX + $LiMnO_2$, using the meta-GGA density functional, r2SCAN; predominance diagram of lanthanum and oxygen chemical potential referenced to their standard elemental state; illustration of the crystallographic analysis of $LaMnO_3$ with respect to space groups *Pnma* vs R3cH; illustration of X-ray diffraction data from in situ synchrotron NSLS II of bulk reaction LaOBr + $LiMnO_2$; and illustration of the crystallographic examination of the evolution of intermediate Mn_3O_4 (PDF)

AUTHOR INFORMATION

Corresponding Author

James R. Neilson — *Department of Chemistry, Colorado State University, Fort Collins, Colorado 80523-1872, United States;* ⓞ orcid.org/0000-0001-9282-5752; Email: james.neilson@colostate.edu

Authors

Gia Thinh Tran — *Department of Chemistry, Colorado State University, Fort Collins, Colorado 80523-1872, United States;* ⓞ orcid.org/0000-0002-3369-7321

Allison Wustrow — *Department of Chemistry, Université de Sherbrooke, Sherbrooke, Quebec J1K 2R1, Canada;* ⓞ orcid.org/0000-0003-1036-9912

Daniel O'Nolan — *Department of Chemistry, Stony Brook University, Stony Brook, New York 11790-3400, United States;* ⓞ orcid.org/0000-0003-1798-3704

SongSheng Tao — *Department of Applied Physics and Applied Mathematics, Columbia University, New York, New York 10027, United States;* ⓞ orcid.org/0000-0002-7565-3503

Christopher J. Bartel — *Chemical Engineering and Materials Science, University of Minnesota, Minneapolis, Minnesota 55455, United States;* ⓞ orcid.org/0000-0002-5198-5036

Tanjin He — *Department of Materials Science and Engineering, University of California, Berkeley, California 94720, United States;* ⓞ orcid.org/0000-0001-8834-8703

Matthew J. McDermott − *Materials Sciences Division, Lawrence Berkeley National Laboratory, Berkeley, California 94720, United States;* ● orcid.org/0000-0002-4071-3000

Brennan C. McBride − *Department of Chemistry, Colorado State University, Fort Collins, Colorado 80523-1872, United States;* ● orcid.org/0000-0002-3825-6138

Karena W. Chapman − *Department of Chemistry, Stony Brook University, Stony Brook, New York 11790-3400, United States;* ● orcid.org/0000-0002-8725-5633

Simon J. L. Billinge − *Department of Applied Physics and Applied Mathematics, Columbia University, New York, New York 10027, United States;* ● orcid.org/0000-0002-9734-4998

Kristin A. Persson − *Molecular Foundry, Lawrence Berkeley National Laboratory, Berkeley, California 94720, United States;* ● orcid.org/0000-0003-2495-5509

Gerbrand Ceder − *Department of Materials Science and Engineering, University of California, Berkeley, California 94720, United States;* ● orcid.org/0000-0001-9275-3605

Complete contact information is available at:
https://pubs.acs.org/10.1021/acs.inorgchem.3c03305

Notes

The authors declare no competing financial interest.

■ REFERENCES

(1) England, W.; Goodenough, J.; Wiseman, P. Ion-exchange reactions of mixed oxides. *J. Solid State Chem.* **1983**, *49*, 289−299.

(2) Hayward, M.; Green, M.; Rosseinsky, M.; Sloan, J. Sodium hydride as a powerful reducing agent for topotactic oxide deintercalation: synthesis and characterization of the nickel (I) oxide LaNiO₂. *J. Am. Chem. Soc.* **1999**, *121*, 8843−8854.

(3) Tsujimoto, Y.; Tassel, C.; Hayashi, N.; Watanabe, T.; Kageyama, H.; Yoshimura, K.; Takano, M.; Ceretti, M.; Ritter, C.; Paulus, W. Infinite-layer iron oxide with a square-planar coordination. *Nature* **2007**, *450*, 1062−1065.

(4) Hayward, M. Topochemical reactions of layered transition-metal oxides. *Semicond. Sci. Technol.* **2014**, *29*, 064010.

(5) Schmalzried, H. *Chemical Kinetics of Solids*; John Wiley & Sons, 2008.

(6) Wustrow, A.; Neilson, J. R. *In Comprehensive Inorganic Chemistry III*, 3rd ed.; Reedijk, J., Poeppelmeier, K. R., Eds.; Elsevier: Oxford, 2023; pp 24−39.

(7) Martinolich, A. J.; Kurzman, J. A.; Neilson, J. R. Polymorph selectivity of superconducting CuSe₂ through kinetic control of solid-state metathesis. *J. Am. Chem. Soc.* **2015**, *137*, 3827−3833.

(8) Todd, P. K.; Neilson, J. R. Selective formation of yttrium manganese oxides through kinetically competent assisted metathesis reactions. *J. Am. Chem. Soc.* **2019**, *141*, 1191−1195.

(9) Todd, P. K.; McDermott, M. J.; Rom, C. L.; Corrao, A. A.; Denney, J. J.; Dwaraknath, S. S.; Khalifah, P. G.; Persson, K. A.; Neilson, J. R. Selectivity in yttrium manganese oxide synthesis via local chemical potentials in hyperdimensional phase space. *J. Am. Chem. Soc.* **2021**, *143*, 15185−15194.

(10) Todd, P. K.; Wustrow, A.; McAuliffe, R. D.; McDermott, M. J.; Tran, G. T.; McBride, B. C.; Boeding, E. D.; O'Nolan, D.; Liu, C.-H.; Dwaraknath, S. S.; et al. Defect-Accommodating intermediates yield selective low-temperature synthesis of YMnO₃ polymorphs. *Inorg. Chem.* **2020**, *59*, 13639−13650.

(11) Wustrow, A.; Huang, G.; McDermott, M. J.; O'Nolan, D.; Liu, C.-H.; Tran, G. T.; McBride, B. C.; Dwaraknath, S. S.; Chapman, K. W.; Billinge, S. J.; et al. Lowering Ternary Oxide Synthesis Temperatures by Solid-State Cometathesis Reactions. *Chem. Mater.* **2021**, *33*, 3692−3701.

(12) Wustrow, A.; McDermott, M. J.; O'Nolan, D.; Liu, C.-H.; Tran, G. T.; McBride, B. C.; Vornholt, S. M.; Feng, C.; Dwaraknath, S. S.; Chapman, K. W.; et al. Reaction Selectivity in Cometathesis: Yttrium Manganese Oxides. *Chem. Mater.* **2022**, *34*, 4694−4702.

(13) Ramirez, A. Colossal magnetoresistance. *J. Phys.: Condens. Matter* **1997**, *9*, 8171−8199.

(14) Töpfer, J.; Goodenough, J. Transport and Magnetic Properties of the Perovskites La₁₋ᵧMnO₃ and LaMn₁₋ᵤO₃. *Chem. Mater.* **1997**, *9*, 1467−1474.

(15) Töpfer, J.; Goodenough, J. LaMnO₃₊δ Revisited. *J. Solid State Chem.* **1997**, *130*, 117−128.

(16) Tofield, B.; Scott, W. Oxidative nonstoichiometry in perovskites, an experimental survey; the defect structure of an oxidized lanthanum Manganite by powder neutron diffraction. *J. Solid State Chem.* **1974**, *10*, 183−194.

(17) Kononova, O.; Huo, H.; He, T.; Rong, Z.; Botari, T.; Sun, W.; Tshitoyan, V.; Ceder, G. Text-mined dataset of inorganic materials synthesis recipes. *Sci. Data* **2019**, *6*, 203.

(18) Mandal, T. K.; Gopalakrishnan, J. From rocksalt to perovskite: a metathesis route for the synthesis of perovskite oxides of current interest. *J. Mater. Chem.* **2004**, *14*, 1273−1280.

(19) Toberer, E. S.; Weaver, J. C.; Ramesha, K.; Seshadri, R. Macroporous monoliths of functional perovskite materials through assisted metathesis. *Chem. Mater.* **2004**, *16*, 2194−2200.

(20) Tarascon, J.; Guyomard, D. Li Metal-Free Rechargeable Batteries Based on Li₁₊ₓMn₂O₄ Cathodes ($0 \leq x \leq 1$) and Carbon Anodes. *J. Electrochem. Soc.* **1991**, *138*, 2864−2868.

(21) Wang, M.; Navrotsky, A. LiMO₂ (M= Mn, Fe, and Co): Energetics, polymorphism and phase transformation. *J. Solid State Chem.* **2005**, *178*, 1230−1240.

(22) O'Nolan, D.; Huang, G.; Kamm, G. E.; Grenier, A.; Liu, C.-H.; Todd, P. K.; Wustrow, A.; Thinh Tran, G.; Montiel, D.; Neilson, J. R.; et al. A thermal-gradient approach to variable-temperature measurements resolved in space. *J. Appl. Crystallogr.* **2020**, *53*, 662−670.

(23) Ashiotis, G.; Deschildre, A.; Nawaz, Z.; Wright, J. P.; Karkoulis, D.; Picca, F. E.; Kieffer, J. The fast azimuthal integration Python library: pyFAI. *J. Appl. Crystallogr.* **2015**, *48*, 510−519.

(24) Pathak, P.; Vasavada, N. Thermal expansion of NaCl, KCl and CsBr by X-ray diffraction and the law of corresponding states. *Acta Crystallogr., Sect. A: Cryst. Phys., Diffr., Theor. Gen. Crystallogr.* **1970**, *26*, 655−658.

(25) Kothakonda, M.; Kaplan, A. D.; Isaacs, E. B.; Bartel, C. J.; Furness, J. W.; Ning, J.; Wolverton, C.; Perdew, J. P.; Sun, J. Testing the r2SCAN Density Functional for the Thermodynamic Stability of Solids with and without a van der Waals Correction. *ACS Mater. Au* **2023**, *3*, 102−111.

(26) Furness, J. W.; Kaplan, A. D.; Ning, J.; Perdew, J. P.; Sun, J. Accurate and numerically efficient r2SCAN meta-generalized gradient approximation. *J. Phys. Chem. Lett.* **2020**, *11*, 8208−8215.

(27) Jain, A.; Ong, S. P.; Hautier, G.; Chen, W.; Richards, W. D.; Dacek, S.; Cholia, S.; Gunter, D.; Skinner, D.; Ceder, G.; et al.

Commentary: The Materials Project: A materials genome approach to accelerating materials innovation. *APL Mater.* **2013**, *1*, 011002.

(28) Kresse, G.; Hafner, J. Ab initio molecular dynamics for liquid metals. *Phys. Rev. B: Condens. Matter Mater. Phys.* **1993**, *47*, 558−561.

(29) Bartel, C. J.; Millican, S. L.; Deml, A. M.; Rumptz, J. R.; Tumas, W.; Weimer, A. W.; Lany, S.; Stevanović, V.; Musgrave, C. B.; Holder, A. M. Physical descriptor for the Gibbs energy of inorganic crystalline solids and temperature-dependent materials chemistry. *Nat. Commun.* **2018**, *9*, 4168.

(30) Yokokawa, H. Generalized chemical potential diagram and its applications to chemical reactions at interfaces between dissimilar materials. *J. Phase Equilib.* **1999**, *20*, 258−287.

(31) Bale, C. W.; Chartrand, P.; Degterov, S.; Eriksson, G.; Hack, K.; Ben Mahfoud, R.; Melançon, J.; Pelton, A.; Petersen, S. FactSage thermochemical software and databases. *CALPHAD* **2002**, *26*, 189−228.

(32) Serpil Gönen, Z.; Gopalakrishnan, J.; Sirchio, S. A.; Eichhorn, B.; Smolyaninova, V.; Greene, R. L. Lithium Substitution in $LaMnO_3$: Synthesis, Structure, and Properties of $LaMn_{1−x}Li_xO3$ Perovskites. *J. Solid State Chem.* **2001**, *159*, 68−71.

(33) Prado, F.; Sánchez, R.; Caneiro, A.; Causa, M.; Tovar, M. Discontinuous evolution of the highly distorted orthorhombic structure and the magnetic order in $LaMnO3±\delta$ perovskite. *J. Solid State Chem.* **1999**, *146*, 418−427.

(34) Miyoshi, S.; Kaimai, A.; Matsumoto, H.; Yashiro, K.; Nigara, Y.; Kawada, T.; Mizusaki, J. In situ XRD study on oxygen-excess $LaMnO_3$. *Solid State Ionics* **2004**, *175*, 383−386.

(35) Neilson, J. R.; McDermott, M. J.; Persson, K. A. Modernist materials synthesis: Finding thermodynamic shortcuts with hyperdimensional chemistry. *J. Mater. Res.* **2023**, *38*, 2885−2893.

(36) Armstrong, A. R.; Bruce, P. G. Synthesis of layered $LiMnO_2$ as an electrode for rechargeable lithium batteries. *Nature* **1996**, *381*, 499−500.

(37) Song, K.; Kauzlarich, S. M. New intercalation compounds of layered lanthanide oxychlorides LnOCl (Ln= Ho, Er, Tm, and Yb) with pyridine and substituted pyridines. *Chem. Mater.* **1994**, *6*, 386−394.

(38) Odink, D. A.; Kauzlarich, S. M. Sodium Intercalation Chemistry of a Novel Host: YbOCl. *Mol. Cryst. Liq. Cryst.* **1990**, *181*, 325−332.

(39) Siol, S.; Holder, A.; Steffes, J.; Schelhas, L. T.; Stone, K. H.; Garten, L.; Perkins, J. D.; Parilla, P. A.; Toney, M. F.; Huey, B. D.; et al. Negative-pressure polymorphs made by heterostructural alloying. *Sci. Adv.* **2018**, *4*, No. eaaq1442.